nature physics

Article

https://doi.org/10.1038/s41567-024-02385-4

The interplay of field-tunable strongly correlated states in a multi-orbital moiré system

Received: 27 March 2023

Accepted: 21 December 2023

Published online: 30 January 2024

Check for updates

Aidan J. Campbell[1], Valerio Vitale[2,3], Mauro Brotons-Gisbert[1], Hyeonjun Baek[4], Antoine Borel[1], Tatyana V. Ivanova[1], Takashi Taniguchi[5,6], Kenji Watanabe[5,6], Johannes Lischner[2] & Brian D. Gerardot[1]

The interplay of charge, spin, lattice and orbital degrees of freedom leads to a variety of emergent phenomena in strongly correlated systems. In transition-metal-dichalcogenide-based moiré heterostructures, recent observations of correlated phases can be described by triangular-lattice single-orbital Hubbard models based on moiré bands derived from the Brillouin-zone corners—the so-called K valleys. Richer phase diagrams described by multi-orbital Hubbard models are possible with hexagonal lattices that host moiré bands at the zone centre—called Γ valleys—or an additional layer degree of freedom. Here we report the tunable interaction between strongly correlated hole states hosted by Γ- and K-derived bands in a heterostructure of monolayer $MoSe_2$ and bilayer 2H WSe_2. We characterize the behaviour of exciton–polarons to distinguish the layer and valley degrees of freedom. The Γ band gives rise to a charge-transfer insulator described by a two-orbital Hubbard model. An out-of-plane electric field re-orders the Γ- and K-derived bands and drives the redistribution of carriers to the layer-polarized K orbital, generating Wigner crystals and Mott insulating states. Finally, we obtain degeneracy of the Γ and K orbitals at the Fermi level and observe interacting correlated states with phase transitions dependent on the doping density. Our results establish a platform to investigate multi-orbital Hubbard model Hamiltonians.

Although conceptually simple, the single-orbital two-dimensional Hubbard model can describe many ingredients of strongly correlated systems. However, real quantum materials are typically described using multi-orbital Hubbard models. For instance, doping in the two-orbital charge-transfer insulator has been connected to high-temperature superconductivity in cuprates[1–3] and iron-based superconductors demand Hubbard models that account for multiple degenerate orbitals at the Fermi level[4]. Although challenges exist to accurately solve the single-orbital Hubbard model and its derivatives, the phase diagrams of more complex multi-orbital models become even more intractable; they sensitively depend on the interplay of the different degrees of freedom[5]. Hence, there is a strong motivation to

[1]Institute of Photonics and Quantum Sciences, SUPA, Heriot-Watt University, Edinburgh, UK. [2]Departments of Materials and Physics and the Thomas Young Centre for Theory and Simulation of Materials, Imperial College London, London, UK. [3]Dipartimento di Fisica, Universitá di Trieste, Trieste, Italy. [4]Department of Physics, Sogang University, Seoul, South Korea. [5]Research Center for Functional Materials, National Institute for Materials Science, Tsukuba, Japan. [6]International Center for Materials Nanoarchitectonics, National Institute for Materials Science, Tsukuba, Japan. e-mail: B.D.Gerardot@hw.ac.uk

https://doi.org/10.1038/s41567-024-02385-4

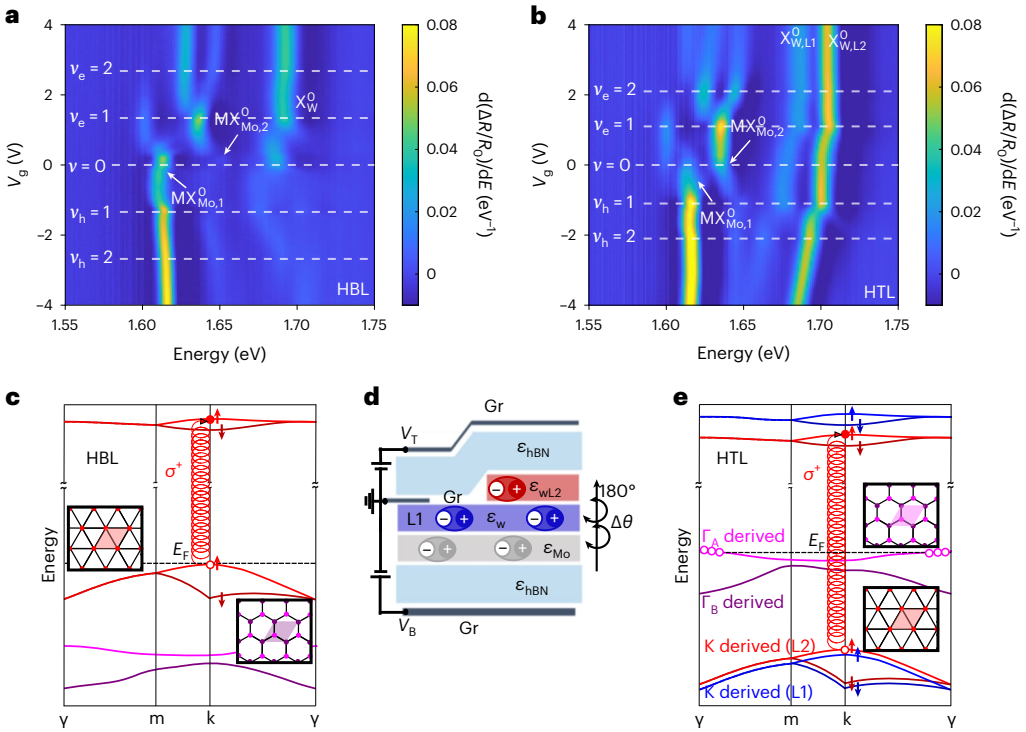

Fig. 1 | Layer and valley properties of excitons and holes in a moiré HTL device. a,**b**, Density plots of the V_g dependence of $d(\Delta R/R_0)/dE$ in the 1L WSe_2/1L $MoSe_2$ (HBL) (**a**) and 2L WSe_2/1L $MoSe_2$ (HTL) (**b**) heterostructure regions. The $MoSe_2$ moiré excitons, namely, $MX_{Mo,1}$ and $MX_{Mo,2}$, and WSe_2 neutral excitons, namely, X^0_W, are indicated. In the HTL, intralayer excitons localized in the interface (L1) and upper (L2) layers of 2L WSe_2 are non-degenerate due to different dielectric environments (ϵ), as indicated in **d**. The white dashed lines indicate integer values of electrons and holes per moiré unit cell, that is, ν_e and ν_h, respectively. **d**, Schematic of the full device with HBL and HTL regions. The TMD layers are fully encapsulated in hBN. Graphene (Gr) layers form contacts to the top and bottom hBN and the heterostructure. **c**,**e**, Schematic of the band structure for the moiré Brillouin zone based on the DFT calculations in the HBL (**c**) and HTL (**e**) regions. In the HBL region, optically injected excitons reside in ±K-derived states and are solely dressed by holes in the ±K moiré orbitals. In the HTL region, the excitons are dressed by holes at both Γ and ±K moiré bands. As indicated in the insets, the Γ moiré orbitals form a honeycomb lattice with inequivalent A and B sites. The moiré orbitals from the ±K valleys form a triangular lattice.

develop platforms for strongly correlated physics that are relatively simple yet possess a high degree of tunability such that emergent physics can be probed and accurately mapped onto paradigmatic quantum Hamiltonians[6,7].

Synthetic moiré superlattices, formed by stacking two atomic layers with a lattice mismatch or a relative twist angle, have emerged as a versatile solid-state platform that potentially fulfils these criteria[7,8]. The versatility of moiré materials arises from the impressive array of tuning knobs that can effectively control the moiré lattice and adjust the strength and nature of the particle interactions. For instance, electrostatic gating can fine-tune the fractional filling (ν) of the lattice with carriers (for electrons or holes, namely, ν_e or ν_h, respectively), displacement fields can adjust the moiré potential depth[9,10] and long-range Coulomb interactions can be manipulated with screening gates[11,12]. Further, in semiconducting transition metal dichalcogenide (TMD)-based moiré systems, the strengths of Coulomb interactions between particles in the moiré lattice can be continuously tuned via the moiré period[13,14]. Additionally, different real-space lattice geometries can be found in the low-energy valence moiré bands, dependent on the valley degree of freedom: moiré orbitals on a triangular lattice are generally found for K-valley moiré bands localized on a single atomic layer[13–19], whereas honeycomb lattices are found for Γ-valley moiré bands spread across each layer[20–27]. In particular, the energetic ordering of Γ- versus K-derived valence moiré bands is sensitively dependent on material combination, twist angle and atomic relaxation effects[28]. To date, most experimental observations of correlated states in both TMD moiré homo- and heterobilayers have been sufficiently described by single-band Hubbard models. Thus, experimentally realizing tunable moiré systems that portray multi-orbital Hubbard physics remains an exciting opportunity in this emerging platform.

Here, by stacking a natural bilayer (2L) of 2H WSe_2 on monolayer (1L) $MoSe_2$ with a relative twist angle to create a heterotrilayer (HTL) device with only one moiré interface, we demonstrate a degree of freedom to realize an extended t–U–V three-orbital Hubbard system based on low-energy moiré bands at Γ and K, which host distinct real-space lattice geometries. Crucially, the relative ordering of these bands can be fine-tuned with an external electric (displacement) field $\vec{E}$ and we are able to investigate the interplay of correlated states between different orbitals. To precisely probe the nature of the correlated states, we develop an optical spectroscopy technique based on the distinctive behaviour of exciton–polarons[29] that unambiguously distinguishes the layer and valley degrees of freedom (Methods).

Layer and valley degrees of freedom for holes in moiré bands

Our HTL sample is a natural 2L of 2H WSe_2/1L $MoSe_2$ device with a moiré interface period of approximately 7 nm due to a relative twist angle of $\theta \approx 2.7 \pm 0.5°$ with respect to R stacking. Compared with a 1L WSe_2/1L $MoSe_2$ HBL device, the HTL provides an additional layer degree of freedom[17,19,30], as well as raising the prospect for exploitation of the valley degree of freedom in the valence band[31]. To aid an unambiguous identification of the spectral features in the HTL device, we investigate a sample (Fig. 1d shows the device schematic) with adjacent HBL and HTL regions with nominally identical moiré period at each WSe_2/$MoSe_2$ interface (Methods). Hence, the HBL serves as a reference with

https://doi.org/10.1038/s41567-024-02385-4

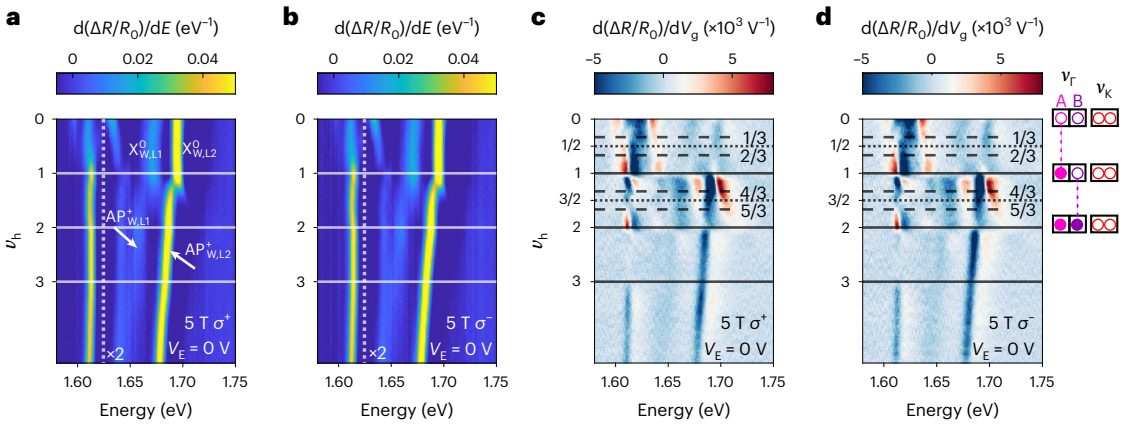

Fig. 2 | Γ-valley correlated hole states in the moiré HTL. a,**b**, σ^+-helicity-resolved (**a**) and σ^--helicity-resolved (**b**) evolution of $d(\Delta R/R_0)/dE$, as a function of ν_h under an applied magnetic field of 5 T. **c**,**d**, Density plot of the first derivative with respect to the gate voltage of $\Delta R/R_0$ ($d(\Delta R/R_0)/dV_g$) in **a** (**c**) and **b** (**d**). The orbital at the Fermi level is depicted in the schematic to the right. On all the plots, the solid lines indicate integer ν_h, whereas the dashed and dotted lines in **c** and **d** show intermediate fractional fillings.

well-understood exciton–polaron behaviour in the presence of strongly correlated states[18].

Figure 1a,b shows doping (V_g)-dependent sweeps (Methods) and monitoring the derivative of the reflection contrast with respect to energy ($d(\Delta R/R_0)/dE$) in the representative HBL and HTL regions of the device, respectively, at a temperature of 4 K. We observe doping-dependent periodic modulations in the peak position, intensity and linewidth of all the intralayer excitonic features at V_g values corresponding to integer ν (Fig. 1a,b, white dashed lines), indicating the formation of correlated electron and hole states. In contrast to the HBL region, in the HTL, we observe two WSe_2 intralayer exciton peaks with different transition energies due to their different dielectric environments (Fig. 1d). The lower-energy feature, labelled $X^0_{W,L1}$, is the WSe_2 neutral exciton localized in the heterostructure interface layer (L1), whereas the higher-energy exciton, that is, $X^0_{W,L2}$, is localized in the top layer (L2) (Methods). This spectroscopic signature provides a clear probe to determine which WSe_2 layer is occupied by the Fermi sea under doping (via the formation of attractive exciton–polarons for each intralayer exciton). The type-II band alignment formed at the interface between L1 WSe_2 and $MoSe_2$ leads to fast non-radiative dephasing and a larger linewidth for $X^0_{W,L1}$ compared with $X^0_{W,L2}$ (ref. 32). Although all data are measured on a single device, we measure multiple spatial locations in the HTL region and find that the behaviour shown here is general (Extended Data Fig. 1 and Extended Data Table 1).

Figure 1c,e shows the schematic of the valence band in the moiré Brillouin zone for HBL and HTL, respectively, based on calculations using ab initio density functional theory (DFT) (Supplementary Discussion 4). Moiré bands derive from either states near the Γ or ±K points. Doped carriers that occupy the valence moiré band arising from ±K form a two-dimensional triangular lattice. In contrast, the holes in the moiré band derived from Γ form a honeycomb lattice with inequivalent A and B sites (Fig. 1e). In addition, the moiré bands inherit the contrasting properties of the different Brillouin-zone locations. Holes in the K-derived bands are highly localized in one of the WSe_2 layers, as shown by the layer distribution of the hole wavefunction (Supplementary Fig. 8), whereas Γ holes are delocalized across both the WSe_2 layers. The Γ_A band is the lowest-energy-available valence moiré band. In each sample, optically excited electron–hole pairs reside in ±K-derived bands, whereas carriers that dress the excitons are doped into the lowest-energy-available valence band, which can be derived from either ±K or Γ. According to the selection rules, for the HTL, σ^+ (σ^-) light probes the +K-derived (−K-derived) states in L1 and the −K-derived (+K-derived) states in L2 of the natural 2L WSe_2, due to 2H stacking and spin-layer locking[33,34].

Probing Γ-valley correlated electronic states

Figure 2a,b shows the σ^+- and σ^--resolved ν_h dependence of the $d(\Delta R/R_0)/dE$ signal, respectively, in the HTL under a 5 T magnetic (B) field. The solid lines indicate integer values of ν_h (that is, the total number of holes per moiré unit cell). To further highlight the formation of correlated electronic states, we plot the derivative of the reflection contrast with respect to V_g, that is, $d(\Delta R/R_0)/dV_g$ (Fig. 2c,d). We note the largest changes in $d(\Delta R/R_0)/dV_g$ (at V_g values of −1.1, −2.1 and −3.1 V) identify the formation of different insulating correlated hole states ($\nu_h = 1$, 2 and 3, respectively). There is a small charge-neutrality region (Extended Data Fig. 6). The V_g value required to fill the moiré lattice with either one electron or one hole per site is identical and corresponds to a twist angle of 2.7° (Methods). We perform temperature-dependent sweeps of V_g and monitor $\Delta R/R_0$ and find a critical temperature $T_c \approx 98$ K for the correlated state at $\nu_h = 1$ and $T_c \approx 59$ K for the correlated state at $\nu_h = 2$ (Extended Data Figs. 4 and 5). We also observe changes in $d(\Delta R/R_0)/dV_g$ at further intermediate hole fillings (Fig. 2c,d, black dashed lines), which we ascribe to the formation of generalized Wigner crystals that arise due to long-range Coulomb interactions[16,30,35]. Although an in-depth understanding about the specific charge and spin ordering of these states is beyond the scope of this work, we refer to recent theoretical works as a starting point to address these issues[22,36–38].

We observe that there is little change in the two WSe_2 excitonic resonance energies as hole doping increases from zero to $\nu_h = 1$. After $\nu_h = 1$, $X^0_{W,L1}$ and $X^0_{W,L2}$ abruptly redshift, indicating the formation of the hole-dressed attractive polarons $AP^+_{W,L1}$ and $AP^+_{W,L2}$ (ref. 39). Three key signatures indicate that the valence-band maximum in the system derives from the Γ valley, as predicted by the DFT calculations (Fig. 1e). First, $AP^+_{W,L1}$ and $AP^+_{W,L2}$ redshift with increasing ν_h. This is in contrast to natural 2L 2H WSe_2, where an overall blueshift in AP^+_W occurs due to Pauli blocking effects: resident carriers fill up the states at the valence band at the ±K point where the photoexcited hole also resides[40] (Supplementary Discussion 2). The contrasting redshift in the moiré HTL implies that the valence-band maximum is not derived from the ±K states. Second, unlike the examples of strong spin polarization of holes residing in ±K valleys[29], in Fig. 2a,b, we observe negligible differences in the intensity and energy of $AP^+_{W,L1}$ and $AP^+_{W,L2}$ between the σ^+- and σ^--resolved sweeps at $B = 5$ T, indicating an absence of spin polarization for the doped holes. This finding is consistent with a photoexcited exciton that resides at ±K dressed by doped holes in moiré bands derived from the Γ point. Finally, $AP^+_{W,L1}$ and $AP^+_{W,L2}$ forming at an identical V_g value is further evidence: holes in the Γ band are delocalized across the two WSe_2 layers and equally dress both $X^0_{W,L1}$ and $X^0_{W,L2}$. In the absence of the delocalization of holes, we would expect carriers

https://doi.org/10.1038/s41567-024-02385-4

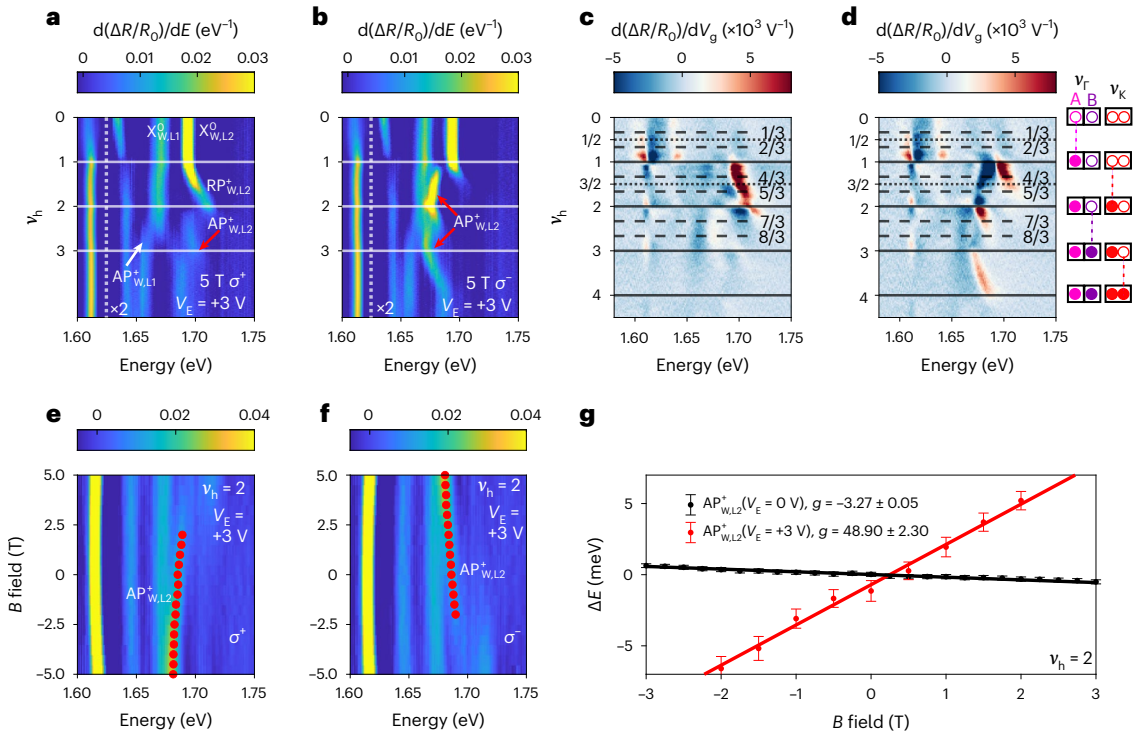

Fig. 3 | Inducing spin and valley polarization in K orbitals with $\vec{E}$. **a**,**b**, ν_h dependence of the σ^+-resolved (**a**) and σ^+-resolved (**b**) $d(\Delta R/R_0)/dE$ at $V_E = +3$ V with $B = 5$ T. **c**,**d**, Density plot of $d(\Delta R/R_0)/dV_g$ in **a** (**c**) and **b** (**d**), which highlight the formation of correlated states (identified by the dashed and solid lines). The orbital at the Fermi level is depicted in the schematic on the right. **e**,**f**, σ^+-resolved (**e**) and σ^--resolved (**f**) B-field sweep of $d(\Delta R/R_0)/dE$ at $V_E = +3$ V and $\nu_h = 2$. The red dots represent the B-field-dependent estimated energies of $AP^+_{W,L2}$. **g**, B-field-dependent Zeeman splitting ΔE of AP^+_W at representative hole values of $\nu_h = 2$ for $V_E = 0$ V (black dots) and $V_E = +3$ V (red dots). For $V_E = +3$ V, ΔE is extracted from the estimated positions shown in **e** and **f**. The g-factor of $AP^+_{W,L2}$ is extracted from linear fits to ΔE (solid lines). The calculated errors represent one standard deviation.

to sequentially fill the L1- and L2-derived moiré bands, causing a V_g offset in the formation of $AP^+_{W,L1}$ and $AP^+_{W,L2}$.

We now discuss the nature of the correlated state that arises at $\nu_h = 1$ in the Γ orbital, which is determined to be a charge-transfer insulator. The energy gap between the two Γ moiré bands that map onto inequivalent A and B sites of a honeycomb lattice (Γ_A and Γ_B orbitals, respectively) is predicted by DFT to be approximately 18 meV (Supplementary Discussion 4), comparable with the value of the charge gap we can tentatively estimate from the temperature at which the correlated state at $\nu_h = 1$ disappears, which is approximately 10 meV (Extended Data Fig. 5). Therefore, the Γ_A lattice is first completely filled, followed by the sequential filling of the Γ_B sites. The inequivalency of the A–B sublattice also presents a probable explanation for the lack of formation of $AP^+_{W,L1}$ and $AP^+_{W,L2}$ up to $\nu_h = 1$. The DFT calculations reveal that the photoexcited hole at K resides on the site of B sublattice, whereas for $0 < \nu_h < 1$, the doped hole in the Γ moiré band lies on the A site (Supplementary Fig. 8). Hence, there is no spatial or momentum overlap between the two states, minimizing the formation of an attractive exciton–polaron[41]. For $1 < \nu_h < 2$, holes are doped into the Γ_B moiré orbital, which spatially overlaps with the photoexcited hole. Hence, attractive polarons form in each layer for this range of ν_h.

Electric-field tuning of moiré orbitals

We now investigate the field tunability of the bands. By probing the magneto-optical properties of WSe_2 exciton–polarons, we disentangle the different spin and valley properties of the holes doped into the Γ and ±K moiré bands as a function of $\vec{E}$, using the tuning knob V_E (Methods provides the definition of V_E). Figure 3a,b shows the polarization-resolved $d(\Delta R/R_0)/dE$ sweeps as a function of ν_h with $B = 5$ T and $V_E = +3$ V. As we increase ν_h in the σ^--resolved spectrum (Fig. 3b), a new resonance (labelled $AP^+_{W,L2}$, indicated by the red arrow) appears at $\nu_h = 1$, ~14 meV lower energy than $X^0_{W,L2}$. This resonance is particularly absent for the σ^+ spectrum (Fig. 3a), where, instead, $X^0_{W,L2}$ evolves into the repulsive-polaron branch $RP^+_{W,L2}$ that blueshifts with increasing doping. The difference in oscillator strengths for $RP^+_{W,L2}$ and $AP^+_{W,L2}$ in the σ^+- and σ^--polarized V_g sweeps indicates a large degree of spin polarization for the carriers that form the exciton–polarons in L2. We, therefore, unambiguously identify $AP^+_{W,L2}$ as the intervalley attractive polaron, which is formed from the direct ±K exciton in L2 dressed with holes in the opposite K valley in L2 (ref. 29). This observation strongly indicates that at $V_E = +3$ V, the L2 K-derived band is tuned upwards in energy relative to the layer-hybridized Γ_B band. Previously, for $V_E = 0$ V and holes loaded only at Γ, there is a complete lack of hole spin polarization, regardless of ν_h (Fig. 2a,b).

Next, we investigate the interaction effects on the magneto-optics for the correlated states in the Γ and K orbitals. Figure 3e,f shows the helicity-resolved evolution of the $d(\Delta R/R_0)/dE$ spectra for applied B fields between −5 and +5 T at $\nu_h = 2$ and $V_E = +3$ V. The B-field-dependent estimated energy of $AP^+_{W,L2}$ extracted from the fits are overlaid in this figure (red dots). Figure 3g shows the Zeeman splitting ΔE of $AP^+_{W,L2}$ versus the B field at $\nu_h = 2$, for both $V_E = 0$ V (black) and $V_E = +3$ V (red), where $\Delta E = E^{\sigma^+} - E^{\sigma^-}$ ($E^{\sigma^\pm}$, transition energy with $\sigma^\pm$ polarization). The evolution of ΔE with B field can be associated with an effective exciton g-factor using $\Delta E(B) = g\mu_0 B$, where μ_0 is the Bohr magneton. For $V_E = 0$ V, when $AP^+_{W,L2}$ is formed by an exciton dressed by holes at Γ, the g-factor is close to −4, which is expected according to spin and valley considerations in the absence of interaction effects[29]. In contrast, for $V_E = +3$ V, $AP^+_{W,L2}$ exhibits a large positive g-factor of approximately 49, partly due to interaction effects that arise from hole doping into

https://doi.org/10.1038/s41567-024-02385-4

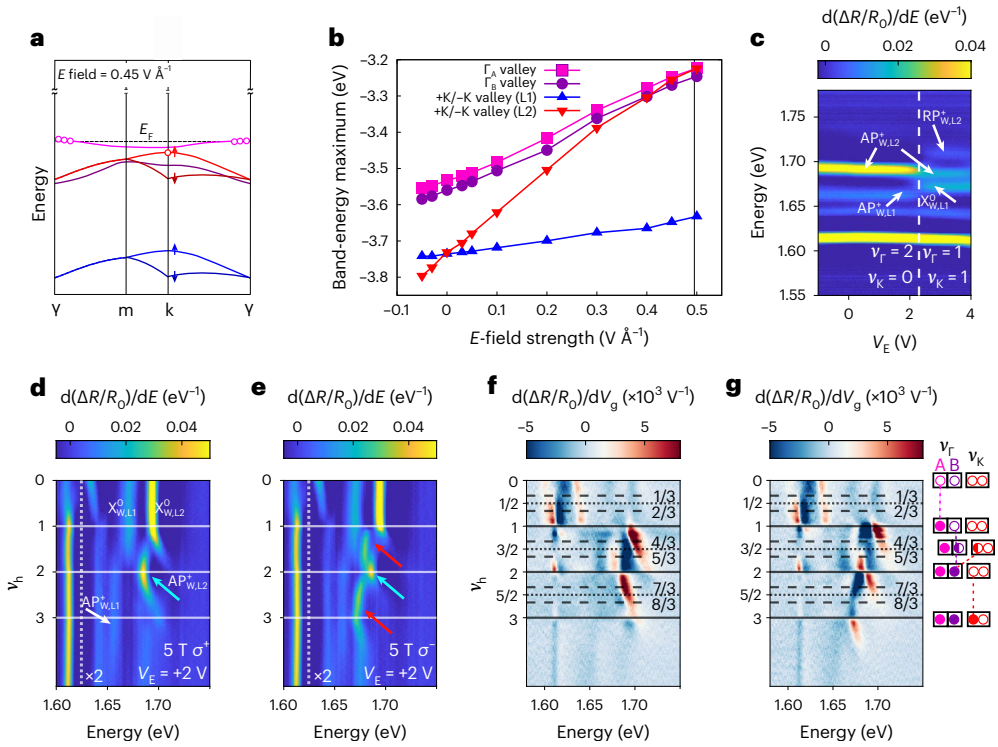

Fig. 4 | Interplay of K- and Γ-valley correlated states. a, Schematic of the band structure for the moiré Brillouin zone based on DFT calculations of the HTL under an applied positive vertical electric (E) field. The K-derived band is shifted to a higher energy relative to the Γ-derived bands compared with $V_E = 0$. **b**, Electric-field dependence of the valence-band maximum for the Γ- and K-derived moiré bands, calculated from DFT. **c**, Density plot of the V_E dependence of the derivative of the $d(\Delta R/R_0)/dE$ when hole filling is fixed at $\nu_h = 2$. The white dashed line indicates an abrupt transfer of holes in the system from the Γ-derived moiré orbital to the K-derived orbital. **d**,**e**, ν_h dependence of the σ^+-resolved (**d**) and σ^--resolved (**e**) $d(\Delta R/R_0)/dE$ at $V_E = +2$ V and $B = 5$ T. **f**,**g**, Density plot of $d(\Delta R/R_0)/dV_g$ for the same data in **d** (**f**) and **e** (**g**), respectively. On all the plots, the solid lines indicate integer ν_h of the moiré superlattice, whereas the dashed and dotted lines in **f** and **g** show intermediate fractional fillings. The schematic on the far right indicates the carriers per moiré unit cell in each of the Γ- or K-derived orbitals, where a filled circle indicates integer filling.

the ±K band and the resulting favoured single-valley occupancy (Extended Data Fig. 3 and Extended Data Table 2)[29]. The measured g-factor is then further enhanced by spin coupling between the moiré localized holes[15,18].

The tuning of the valence bands in the system is further demonstrated by the suppression of the formation of the attractive polaron for the L1 WSe_2 exciton, that is, AP^+_{L1}, up to $\nu_h > 2$: holes are doped into the highly localized L2 K band and therefore have little effect on the L1 WSe_2 exciton. Finally, we note that the binding energy E_B for the hole-dressed attractive polaron formed by the L2-localized exciton for $V_E = +3$ V ($E_B \approx 14$ meV) is much larger than the binding energy for $V_E = 0$ V ($E_B \approx 6$ meV). This result is consistent with a larger wavefunction overlap between the exciton at ±K dressed by holes at ∓K compared with holes at Γ.

Correlated states: Γ versus K orbitals

We now investigate the correlated states formed within the Γ and K orbitals. We expect the same dependence of V_g versus ν_h for each orbital. Figure 3c,d shows the ν_h dependence of $d(\Delta R/R_0)/dV_g$ for the same data in Fig. 3a,b, respectively. As expected, we observe the largest changes in the $d(\Delta R/R_0)/dV_g$ signal at integer ν_h and smaller changes at intermediate ν_h, as previously observed for $V_E = 0$ V (Fig. 2c,d). However, we observe that new correlated states emerge for $V_E = +3$ V compared with $V_E = 0$ V. A new state at $\nu_h = 4$ clearly appears, as well as further states at $\nu_h = 7/3$ and 8/3.

To understand the origin of the additional correlated insulating states, we again use the polarization-resolved doping-dependent reflection contrast measurements (Figs. 2a,b and 3a,b) and assign the correlated states to filling of either the Γ or K orbitals, as indicated by the schematics on the far right in these figures. For $\nu_h < 1$, we observe that attractive polarons do not form for any V_E because holes are always doped first into the Γ_A orbital. We then observe that $AP^+_{W,L2}$ and $RP^+_{W,L2}$ form at $\nu_h > 1$ with a large spin polarization, demonstrating doping into the K orbital. Hence, for $V_E = +3$ V at $\nu_h = 2$, a correlated state arises in which the lower Hubbard bands are filled for both Γ_A and K orbitals. In contrast, for $V_E = 0$ V and $1 < \nu_h < 2$, the Γ_B orbital is filled, as demonstrated by the lack of spin polarization of the carriers that form $AP^+_{W,L1}$ and $AP^+_{W,L2}$ (Fig. 2a,b).

Continuing with the $V_E = +3$ V scenario, after $\nu_h = 2$, the non-spin-polarized $AP^+_{W,L1}$ forms because holes are now doped into the Γ_B orbital. Hence, at $\nu_h = 3$, a correlated state arises in which each orbital (Γ_A, Γ_B and K) is filled with one hole. Finally, for $\nu_h > 3$, $AP^+_{W,L2}$ continually blueshifts with increasing doping, indicating Pauli blocking effects arising from doping into the K orbital, whereas $AP^+_{W,L1}$ remains unaffected. At $\nu_h = 4$, we, therefore, have a correlated state with $\nu_\Gamma = 2$ and $\nu_K = 2$. These assignments are consistent with the emergence of new states at $\nu_h = 7/3$ and 8/3 for $V_E = +3$ V. In comparison, for $V_E = 0$ V, the Wigner crystals driven by long-range interactions are not observed at these ν_h values in the next Γ moiré orbital. The emergence of new correlated states at $\nu_h = 7/3$, 8/3 and 4 is consistent with metal–insulator transitions occurring at these ν_h values, driven by V_E-dependent tuning of the relative Γ–K-band energies.

Interplay of correlated states between degenerate orbitals

To better understand the V_E-dependent shifts in the K and Γ_B orbitals, we perform DFT calculations for the HTL in the presence of a vertical electric field. Figure 4a shows a simplified schematic of the band

https://doi.org/10.1038/s41567-024-02385-4

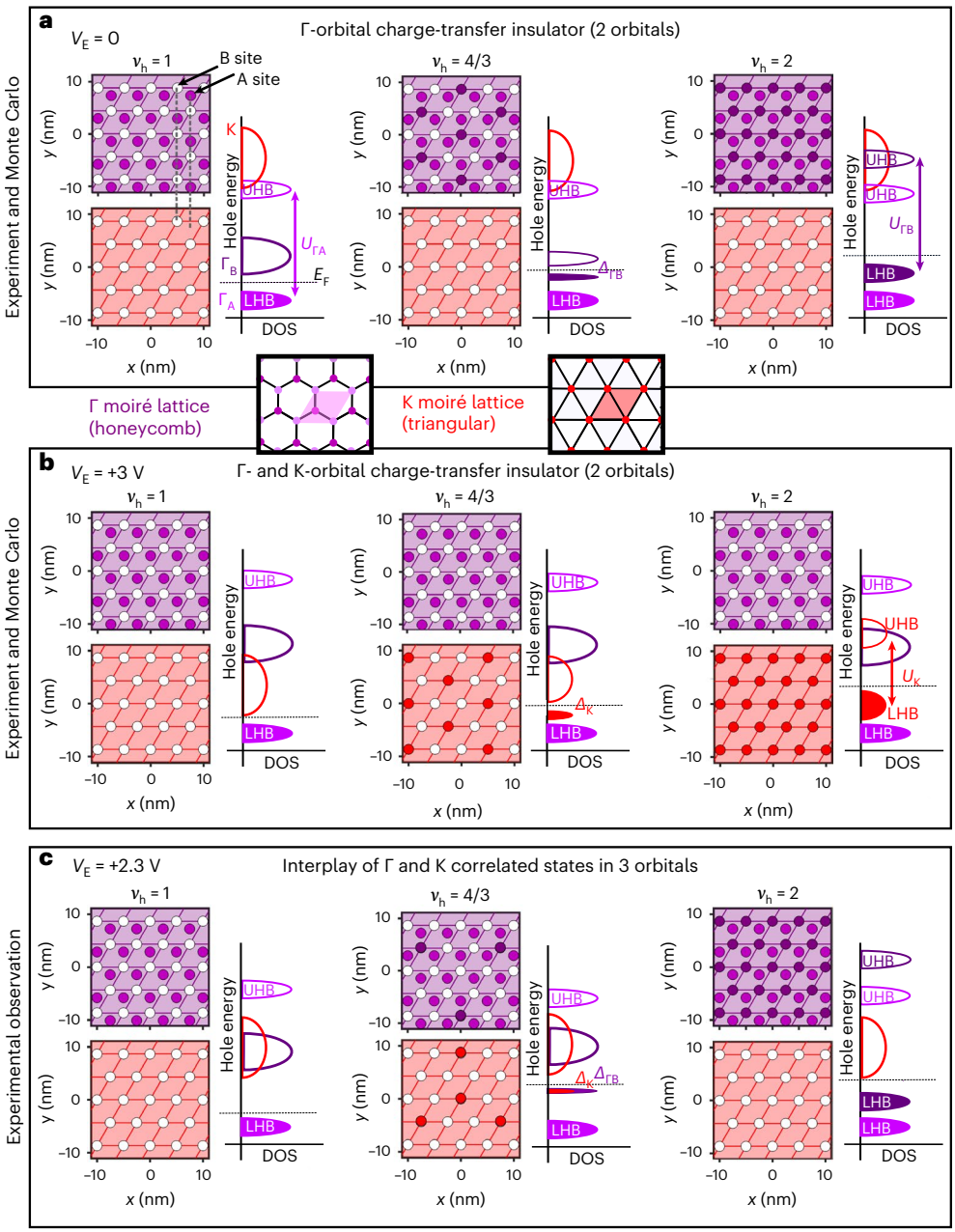

Fig. 5 | Real-space charge distributions of correlated states in the Γ_A, Γ_B and K orbitals at select values of ν_h and V_E. a, Charge-ordered states (formulated using Monte Carlo simulations) that arise in the Γ (pink and purple) and K (red) moiré lattices for $V_E = 0$, for which the energy of the K-derived band is below both Γ-derived bands ($\epsilon_K < \epsilon_B$). The Γ_B sites are spatially aligned with the K sites in the x–y plane. Holes are first loaded into the Γ_A sites up to $\nu_h = 1$ and into the Γ_B sites for $\nu_h > 1$. Schematic to the right illustrates the hole energy versus density of states (DOS) for each charge-ordered state shown in these data. The lower Hubbard band (LHB) and upper Hubbard band (UHB) form for $\nu_h = 1$, whereas a charge gap Δ opens up for correlated states that form for non-integer filling. **b**, Charge-ordered states (formulated using Monte Carlo simulations) and the corresponding DOS schematic that arises for $V_E = +3$ V, for which the energy of the K orbital lies between the Γ orbitals ($\epsilon_A > \epsilon_K > \epsilon_B$). Holes are first loaded into the Γ_A sites up to $\nu_h = 1$ and into K for $\nu_h > 1$. **c**, Experimentally observed charge-ordered states and corresponding DOS schematics for $V_E = +2.3$ V for which the K orbital is energetically degenerate with the Γ_B orbital. Holes are first loaded into the Γ_A sites up to $\nu_h = 1$, and into both K and Γ_B for $\nu_h > 1$. At $\nu_h = 2$, holes are abruptly transferred from K to Γ_B to form the correlated state with $\nu_{\Gamma A} = 1$ and $\nu_{\Gamma B} = 1$.

structure in the moiré Brillouin zone for a positive vertical electric field (Supplementary Discussion 4 shows the calculated full band structure). In agreement with the experiment, we observe that the ±K-derived bands localized on L2 are pushed up in energy (that is, reduced hole energy) relative to the Γ_B bands (Fig. 1e shows a comparison). Figure 4b shows the band-edge energy of the Γ_A, Γ_B, L1 K and L2 K bands as function of the applied electric-field strength. Due to the high localization of its wavefunction on L2 WSe_2 (Supplementary Fig. 7), the L2 K orbital exhibits the largest V_E-dependent shift in energy. In contrast, the Γ_A and Γ_B bands exhibit smaller V_E-dependent energy shifts due to delocalization across both WSe_2 layers[31].

To probe the interplay between correlated states in Γ and K orbitals in more detail, we measure the V_E dependence of the $d(\Delta R/R_0)/dE$ signal for a fixed hole filling of $\nu_h = 2$ (Fig. 4c). For $V_E = 0$ V, we observe the two WSe_2 attractive polaron resonances: intralayer excitons localized in L1 and L2 of the bilayer dressed by delocalized holes residing in the highest Γ moiré miniband ($AP^+_{W,L1}$ and $AP^+_{W,L2}$, respectively). However, as V_E increases, these features are abruptly replaced by three new resonances

at $V_E \approx 2.3$ V. The full-width at half-maximum of the change in the $d(\Delta R/R_0)/dE$ signal is calculated to be $\Delta V_E = 0.53$ V (Extended Data Fig. 2). To identify the origin of the abrupt change, we measure the helicity-resolved ν_h dependence of $d(\Delta R/R_0)/dE$ with $V_E = +2$ V and $B = 5$ T (Fig. 4d,e). Figure 4f,g shows the ν_h dependence of $d(\Delta R/R_0)/dV_g$ for the same data. Identical to the case for $V_E = +3$ V, in the σ^- spectrum (Fig. 4d), we observe the emergence of a new highly spin-polarized resonance $AP^+_{W,L2}$ (red arrow), indicating that holes are initially doped into the L2 K moiré band for $\nu_h > 1$. However, for σ^-, at around $\nu_h = 2$, the oscillator strength is transferred to a higher-energy feature with a smaller binding energy, which also appears for the σ^+-resolved data (Fig. 4d, blue arrows). This feature lacks a strong degree of spin polarization, suggesting that holes are transferred from the K to the Γ_B orbital at $\nu_h = 2$. The hole transfer is further demonstrated by the formation of an attractive polaron for the L1 WSe_2 exciton at around $\nu_h = 2$, at the same hole filling where the transfer of oscillator strength occurs. For $\nu_h > 2$, holes start to be doped into the K orbital again, and the spin-polarized features re-emerge. Therefore, we assign the abrupt change in the absorption spectrum at $V_E = +2.3$ V (Fig. 4c) to a transfer of holes from the Γ_B to the K moiré orbital.

Rather than being continuous, the observed change occurs over a small range of V_E ($\Delta V_E \approx 0.5$ V). If holes were continuously transferred between the orbitals, there would be a gradual change in oscillator strength[17]. Instead, the abrupt change indicates that the system favours the formation of a correlated state, and the different V_E-dependent scenarios for $\nu_h = 2$ provide an archetypal illustration. For a small V_E, a correlated state with $\nu_h = 1$ in each Γ_A and Γ_B orbit arises. For large V_E, a correlated state with $\nu_h = 1$ in the Γ_A orbital and $\nu_h = 1$ in the K orbital is formed. However, when the Γ_B and K orbitals are nearly degenerate at the Fermi level, the holes preferentially transfer from the K orbital to the Γ_B orbital, probably due to a larger Coulomb gap for the filled Γ_B orbital, which minimizes the energy of the correlated state. A summary of the orbital filling near degeneracy is depicted as a schematic (Fig. 4g, right).

Discussion

In the experiment, we observe an interplay between correlated states in three orbitals, which can be tuned with V_E. Here we apply a t–U–V Hamiltonian in the $t/U \to 0$ limit (Methods) to provide a more detailed picture of the charge ordering and interactions of these correlated states. Charges can be distributed (and redistributed) between the Γ_A, Γ_B and K orbitals as hole filling increases. It is probable that complex correlated states with specific charge ordering in real space arise to minimize electrostatic repulsion for a given ν_h, similar to that observed in bilayer Hubbard model physics[19].

First, we model the trilayer with $V_E = 0$, where the onsite energy for the L2 K orbital (ε_K) is much larger than both Γ_A and Γ_B onsite orbital energies (ε_A and ε_B, respectively). For $\nu_h = 1$, the holes occupy the Γ_A orbitals, forming a triangular lattice (Fig. 5a). This correlated state is characterized by an occupied lower hole Hubbard band, which is separated from the upper hole Hubbard band by the onsite Coulomb energy U_{Γ_A} (Fig. 5a). Further hole doping results in the occupancy of the Γ_B sites as well as the formation of charge-ordered Γ_B states, consistent with the experimental findings of the Γ-derived Wigner crystal at $\nu_h = 4/3$ (Fig. 2c,d). At $\nu_h = 2$, all the Γ_A and Γ_B sites are occupied, whereas the L2 K orbital remains empty.

Next, we consider the case of a large electric field, namely, $V_E = +3$ V, with $\varepsilon_B > \varepsilon_K > \varepsilon_A$ and for $\nu_h = 1$, the holes still occupy the Γ_A sites. Further hole doping, however, results in the L2 K orbital becoming occupied and forming charge-ordered states (Fig. 5b), consistent with the experimental picture of B-field-dependent correlated states at $\nu_h = 4/3$. At $\nu_h = 2$, the lower Hubbard bands of the Γ_A and L2 K orbitals are fully occupied by holes, whereas the upper Hubbard bands are empty.

Finally, we consider the critical electric field, namely, $V_E = +2.3$ V. At this field, $\varepsilon_B \approx \varepsilon_K > \varepsilon_A$ and we expect strong quantum interaction effects to occur, which are not captured by our electrostatic model. For $\nu_h = 1$, the holes still occupy the Γ_A sites. As a result of the degeneracy of the Γ_B and L2 K orbitals, we hypothesize that additional holes ($1 < \nu_h < 2$) occupy both orbitals to minimize the overall Coulomb repulsion (Fig. 5c). When the doping reaches $\nu_h = 2$, we experimentally observe that all the holes reside in Γ-derived states. This can be explained by the formation of a correlated state in which the lower Hubbard bands for both Γ_A and Γ_B orbitals are fully occupied. As the bandwidth of the Γ-derived bands is smaller than that of the K-derived bands (according to DFT calculations), it is energetically favourable for the Γ orbitals to be fully occupied. Thus, the holes spontaneously redistribute from the K to Γ_B orbital. This observation provides motivation for future theoretical and experimental investigations to fully understand the many-body physics of this strongly correlated multi-orbital system.

Online content

Any methods, additional references, Nature Portfolio reporting summaries, source data, extended data, supplementary information, acknowledgements, peer review information; details of author contributions and competing interests; and statements of data and code availability are available at https://doi.org/10.1038/s41567-024-02385-4.

References

1. Emery, V. Theory of high-T_c superconductivity in oxides. *Phys. Rev. Lett.* **58**, 2794 (1987).
2. Zhang, F. & Rice, T. Effective Hamiltonian for the superconducting Cu oxides. *Phys. Rev. B* **37**, 3759 (1988).
3. Dagotto, E. Correlated electrons in high-temperature superconductors. *Rev. Mod. Phys.* **66**, 763 (1994).
4. Dai, P., Hu, J. & Dagotto, E. Magnetism and its microscopic origin in iron-based high-temperature superconductors. *Nat. Phys.* **8**, 709–718 (2012).
5. Rohringer, G. et al. Diagrammatic routes to nonlocal correlations beyond dynamical mean field theory. *Rev. Mod. Phys.* **90**, 025003 (2018).
6. Gross, C. & Bloch, I. Quantum simulations with ultracold atoms in optical lattices. *Science* **357**, 995–1001 (2017).
7. Kennes, D. M. et al. Moiré heterostructures as a condensed-matter quantum simulator. *Nat. Phys.* **17**, 155–163 (2021).
8. Mak, K. F. & Shan, J. Semiconductor moiré materials. *Nat. Nanotechnol.* **17**, 686–695 (2022).
9. Ghiotto, A. et al. Quantum criticality in twisted transition metal dichalcogenides. *Nature* **597**, 345–349 (2021).
10. Li, T. et al. Continuous Mott transition in semiconductor moiré superlattices. *Nature* **597**, 350–354 (2021).
11. Stepanov, P. et al. Untying the insulating and superconducting orders in magic-angle graphene. *Nature* **583**, 375–378 (2020).
12. Li, T. et al. Charge-order-enhanced capacitance in semiconductor moiré superlattices. *Nat. Nanotechnol.* **16**, 1068–1072 (2021).
13. Wu, F., Lovorn, T., Tutuc, E. & MacDonald, A. H. Hubbard model physics in transition metal dichalcogenide moiré bands. *Phys. Rev. Lett.* **121**, 026402 (2018).
14. Zhang, Y., Yuan, N. F. & Fu, L. Moiré quantum chemistry: charge transfer in transition metal dichalcogenide superlattices. *Phys. Rev. B* **102**, 201115 (2020).
15. Tang, Y. et al. Simulation of Hubbard model physics in WSe_2/WS_2 moiré superlattices. *Nature* **579**, 353–358 (2020).
16. Regan, E. C. et al. Mott and generalized Wigner crystal states in WSe_2/WS_2 moiré superlattices. *Nature* **579**, 359–363 (2020).
17. Shimazaki, Y. et al. Strongly correlated electrons and hybrid excitons in a moiré heterostructure. *Nature* **580**, 472–477 (2020).
18. Campbell, A. J. et al. Exciton-polarons in the presence of strongly correlated electronic states in a $MoSe_2/WSe_2$ moiré superlattice. *npj 2D Mater. Appl.* **6**, 79 (2022).
19. Xu, Y. et al. A tunable bilayer Hubbard model in twisted WSe_2. *Nat. Nanotechnol.* **17**, 934–939 (2022).

20. Angeli, M. & MacDonald, A. H. Γ valley transition metal dichalcogenide moiré bands. *Proc. Natl Acad. Sci. USA* **118**, e2021826118 (2021).
21. Xian, L. et al. Realization of nearly dispersionless bands with strong orbital anisotropy from destructive interference in twisted bilayer MoS_2. *Nat. Commun.* **12**, 5644 (2021).
22. Kaushal, N., Morales-Durán, N., MacDonald, A. H. & Dagotto, E. Magnetic ground states of honeycomb lattice Wigner crystals. *Commun. Phys.* **5**, 289 (2022).
23. An, L. et al. Interaction effects and superconductivity signatures in twisted double-bilayer WSe_2. *Nanoscale Horiz.* **5**, 1309–1316 (2020).
24. Pei, D. et al. Observation of Γ-valley moiré bands and emergent hexagonal lattice in twisted transition metal dichalcogenides. *Phys. Rev. X* **12**, 021065 (2022).
25. Gatti, G. et al. Flat Γ moiré bands in twisted bilayer WSe_2. *Phys. Rev. Lett.* **131**, 046401 (2023).
26. Foutty, B. A. et al. Tunable spin and valley excitations of correlated insulators in Γ-valley moiré bands. *Nat. Mater.* **22**, 731–736 (2023).
27. Magorrian, S. et al. Multifaceted moiré superlattice physics in twisted WSe_2 bilayers. *Phys. Rev. B* **104**, 125440 (2021).
28. Vitale, V., Atalar, K., Mostofi, A. A. & Lischner, J. Flat band properties of twisted transition metal dichalcogenide homo- and heterobilayers of MoS_2, $MoSe_2$, WS_2 and WSe_2. *2D Mater.* **8**, 045010 (2021).
29. Back, P. et al. Giant paramagnetism-induced valley polarization of electrons in charge-tunable monolayer $MoSe_2$. *Phys. Rev. Lett.* **118**, 237404 (2017).
30. Zhou, Y. et al. Bilayer Wigner crystals in a transition metal dichalcogenide heterostructure. *Nature* **595**, 48–52 (2021).
31. Movva, H. C. et al. Tunable Γ-K valley populations in hole-doped trilayer WSe_2. *Phys. Rev. Lett.* **120**, 107703 (2018).
32. Rigosi, A. F., Hill, H. M., Li, Y., Chernikov, A. & Heinz, T. F. Probing interlayer interactions in transition metal dichalcogenide heterostructures by optical spectroscopy: MoS_2/WS_2 and $MoSe_2/WSe_2$. *Nano Lett.* **15**, 5033–5038 (2015).
33. Jones, A. M. et al. Spin–layer locking effects in optical orientation of exciton spin in bilayer WSe_2. *Nat. Phys.* **10**, 130–134 (2014).
34. Brotons-Gisbert, M. et al. Spin-layer locking of interlayer excitons trapped in moiré potentials. *Nat. Mater.* **19**, 630–636 (2020).
35. Xu, Y. et al. Correlated insulating states at fractional fillings of moiré superlattices. *Nature* **587**, 214–218 (2020).
36. Kaushal, N. & Dagotto, E. Moiré Kanamori-Hubbard model for transition metal dichalcogenide homobilayers. *Phys. Rev. B* **107**, L201118 (2023).
37. Morales-Durán, N., Potasz, P. & MacDonald, A. H. Magnetism and quantum melting in moiré-material Wigner crystals. *Phys. Rev. B* **107**, 235131 (2023).
38. Matty, M. & Kim, E.-A. Melting of generalized Wigner crystals in transition metal dichalcogenide heterobilayer moiré systems. *Nat. Commun.* **13**, 7098 (2022).
39. Courtade, E. et al. Charged excitons in monolayer WSe_2: experiment and theory. *Phys. Rev. B* **96**, 085302 (2017).
40. Wang, Z., Chiu, Y.-H., Honz, K., Mak, K. F. & Shan, J. Electrical tuning of interlayer exciton gases in WSe_2 bilayers. *Nano Lett.* **18**, 137–143 (2018).
41. Naik, M. H. et al. Intralayer charge-transfer moiré excitons in van der Waals superlattices. *Nature* **609**, 52–57 (2022).

Methods

Exciton–polaron spectroscopy of correlated states with layer and valley specificity

To precisely probe the nature of the correlated states, we develop an optical spectroscopy technique that yields unambiguous layer- and valley-specific experimental signatures. We probe momentum-direct electrons and holes at ±K valleys that form tightly bound intralayer excitons, which are extremely sensitive to their environment. The binding energy of the exciton depends on its dielectric environment[42], leading to layer-specific exciton energies[43], whereas excitons dressed by a Fermi sea form attractive exciton–polarons (AP) and repulsive exciton–polarons (RP)[44,45], which exhibit distinct behaviours depending on the valley hosting the Fermi sea. For doping at ±K, dominant phase-space-filling effects cause an overall blueshift in the AP[29], whereas doping in the Γ valley leads to a continuous redshift due to bandgap renormalization[46]. Contrasting properties in an applied magnetic field also manifest for excitons dressed by carriers in the two valleys: unlike Γ-valley holes, K-valley holes are highly spin polarized and exhibit strong magnetic interactions with excitons at ±K (ref. 29). Finally, the formation of strongly correlated states leads to abrupt changes in the oscillator strength, energy and linewidth of the exciton–polarons, regardless of which valley the Fermi sea occupies[15,17,18]. Altogether, exciton–polarons provide probes of strongly correlated electronic states with layer and valley specificity.

Device details

The moiré region in the heterostructure is fully encapsulated in hexagonal boron nitride (hBN). There are few-layer graphene contacts to both top and bottom hBN, as well as the heterostructure that allows the carrier concentration and vertical electric field to be independently tuned (Fig. 1b). To change the carrier concentration in the heterostructure without changing the vertical electric field, we sweep both V_T and V_B with the same values, that is, $V_T = V_B = \Delta V_g$. To change the vertical electric field without changing the carrier concentration, $V_T = -V_B = V_E$. The applied vertical electric field can then be calculated using $E = \frac{(V_T - V_B)}{(d_1 + d_2)} \frac{\epsilon_{hBN}}{\epsilon_{TMD}}$. For intermediate regimes, when we want to change both applied vertical electric field and carrier concentration, we apply asymmetric gating, that is, $V_T \neq V_B$.

To experimentally calibrate ν_h, we identify the first three largest changes in the $d(\Delta R/R_0)/dV_g$ signal. We find that for each applied V_E, the dashed lines are equidistant in ΔV_g. Hence, we assign them to be $\nu_h = 1$, 2 and 3. We observe that the calibrated values exhibit a slight V_g offset from $V_g = 0$ V for the charge-neutrality region ($\nu_h = 0$) in the device, and the V_g offset becomes larger for increasing V_E. The carrier concentration n in the heterostructure can be calculated using the parallel-plate capacitor model, that is, $n = \frac{\epsilon\epsilon_0 \Delta V_g}{d_1} + \frac{\epsilon\epsilon_0 \Delta V_g}{d_2}$, where ϵ is the permittivity of hBN, ΔV_g is the voltage offset between both top and bottom gates and heterostructure gate and d_1 (d_2) is the thickness of the top (bottom) hBN layer and measured to be 17.4 ± 0.2 nm (18.2 ± 0.3 nm) using nulling ellipsometry. For a small angular difference between two stacked layers, the moiré periodicity can be estimated using $\lambda_M = \frac{a_{Se}}{\sqrt{\delta^2 + \theta^2}}$, where a_{Se} is the lattice constant of WSe_2, δ is the fractional lattice mismatch between the two layers and θ is the twist angle in radians. For a triangular moiré pattern (or honeycomb with inequivalent A and B sites, where only one site is doped), the number of carriers required for one hole per site is given by $n_0 = \frac{2}{\sqrt{3}\lambda_M^2}$. Using the lattice constants of 0.3280 and 0.3288 nm for WSe_2 and $MoSe_2$, respectively[47]; permittivity of 3.8 for hBN (ref. 48); and $\Delta V_g = 1.00$ V for $\nu_h = 1$ (as determined in the main text), we calculate the twist angle in the main measurement location to be 2.7°. We determine that the interface in HTL is R stacked as a result of the fabrication process. Single flakes of $MoSe_2$ and WSe_2 with monolayer and natural 2H bilayer regions are first exfoliated with the terraced layers (flat surface) facing up (on the substrate). The WSe_2 flake (terraced side up) is then transferred onto $MoSe_2$ on its substrate, keeping the interface between the two layers free from contaminants. The HBL region is H stacked, as demonstrated by magneto-optical studies on the same sample[49,50] and polarization-resolved second-harmonic generation measurements (Supplementary Discussion 1), whereas in the HTL region, the WSe_2 interface layer L1 is R stacked relative to 1L $MoSe_2$. The upper WSe_2 layer L2 is, therefore, H stacked relative to 1L $MoSe_2$. We note that second-harmonic generation measurements cannot be used to determine R versus H stacking of the HTL heterointerface. DFT calculations show that both R- and H-stacked interfaces lead to qualitatively identical band structures with ground-state Γ-derived moiré bands with a honeycomb lattice (Extended Data Fig. 7).

Optical spectroscopy measurements

We focus a broadband white-light source from a power-stabilized halogen lamp onto the sample, and measure the reflected signal in a liquid-nitrogen-cooled charge-coupled device spectrometer. The sample is mounted in a closed-cycle cryostat and the sample temperature for all the experiments in the main text is 4 K. We define the reflection contrast as $\Delta R/R_0$, where $\Delta R = (R_S - R_0)/R_0$. Here R_S is the reflected signal from the heterostructure and R_0 is the reflected signal from a nearby heterostructure region without the TMD layers. Since we use the change in the $d(\Delta R/R_0)/dV_g$ signal to identify the correlated states, excitons with a larger oscillator strength and hence higher $\Delta R/R_0$ signal exhibit a larger change in $d(\Delta R/R_0)/dV_g$.

DFT calculations

The moiré unit cell for the free-standing 2H $WSe_2/MoSe_2$ HTL with a twist angle of 3.1° contains 2,979 atoms. To calculate the band structure, we first relax the atomic positions using classical force fields as implemented in the LAMMPS code[51] (Supplementary Discussion 4 provides details on the HTL geometry and atomic relaxations). DFT calculations were carried out on the relaxed structure using the linear-scaling DFT code SIESTA[52]. We employ the local-density-approximation exchange–correlation functional[53], with a double-zeta plus polarization pseudo-atomic orbital basis set, a mesh cutoff of 300 Ry and a vacuum region between periodic images of 15 Å. Spin–orbit coupling was included via the 'onsite' approximation[54]. Electron–ion interactions are described by fully relativistic Troulliers–Martins pseudopotentials[55].

For calculations with a non-zero vertical electric field, the same atomic positions as in the zero-field case are used, and we employ a slab dipole correction, in which the electric field used to compensate the dipole of the system is self-consistently computed in every iteration[56]. Supplementary Discussion 4 reports the DFT band structures with and without the electric field as well as selected wavefunctions of Γ-valley and ±K-valley bands.

t–*U*–*V* Hamiltonian

We analyse a three-orbital t–U–V Hamiltonian in the $t/U \to 0$ limit. In this limit, each moiré site can be occupied by at most one hole and no hopping between moiré sites is allowed. To find which configuration of holes n_i (where i labels the various moiré sites corresponding to L2 K, Γ_A and Γ_B orbitals) minimizes the total energy, we use an annealing approach formulated using Monte Carlo simulations. The total energy is given by

$$H = \varepsilon_A \sum_{i \in \Gamma_A} n_i + \varepsilon_B \sum_{i \in \Gamma_B} n_i + \varepsilon_K(V_E) \sum_{i \in K} n_i + \frac{1}{2} \sum_{i,j \in \{\Gamma_A, \Gamma_B, K\}} V(|\mathbf{r}_i - \mathbf{r}_j|) n_i n_j, \quad (1)$$

where ε_A, ε_B and $\varepsilon_K(V_E)$ denote the onsite energies of the Γ_A, Γ_B and L2 K orbitals, respectively. Note that the onsite energy of the L2 K orbital

(relative to that of Γ orbitals) depends on the applied electrostatic potential V_E. From our DFT calculations, we estimate $\varepsilon_A - \varepsilon_B \approx 20$ meV, independent of V_E. Also, $V(|\mathbf{r}_i - \mathbf{r}_j|) = \frac{\exp(-|\mathbf{r}_i-\mathbf{r}_j|/L_0)}{\epsilon|\mathbf{r}_i-\mathbf{r}_j|}$ denotes the screened Yukawa interaction between the holes located at positions $\mathbf{r}_i$ and $\mathbf{r}_j$, where ϵ is the dielectric constant (which we set to 4.5) and L_0 is the characteristic screening length (which we set to 2 nm). As the K-derived states are highly localized on the L2 WSe_2 layer, the corresponding hole positions are assumed to lie in the plane of the layer. In contrast, our DFT calculations show that the Γ-derived states are delocalized across both WSe_2 layers, and we, therefore, assume that the corresponding hole positions lie at the midpoint between the layers.

Data availability

The dataset generated and analysed during the current study is available at https://doi.org/10.17861/f4e79017-4043-4318-9315-0793e1fddabc. Source data are provided with this paper.

References

42. Raja, A. et al. Coulomb engineering of the bandgap and excitons in two-dimensional materials. *Nat. Commun.* **8**, 15251 (2017).
43. Chen, D. et al. Excitonic insulator in a heterojunction moiré superlattice. *Nat. Phys.* **18**, 1171–1176 (2022).
44. Sidler, M. et al. Fermi polaron-polaritons in charge-tunable atomically thin semiconductors. *Nat. Phys.* **13**, 255–261 (2017).
45. Efimkin, D. K. & MacDonald, A. H. Many-body theory of trion absorption features in two-dimensional semiconductors. *Phys. Rev. B* **95**, 035417 (2017).
46. Gao, S., Liang, Y., Spataru, C. D. & Yang, L. Dynamical excitonic effects in doped two-dimensional semiconductors. *Nano Lett.* **16**, 5568–5573 (2016).
47. Brixner, L. H. Preparation and properties of the single crystalline AB2-type selenides and tellurides of niobium, tantalum, molybdenum and tungsten. *J. Inorg. Nucl. Chem.* **24**, 257–263 (1962).
48. Laturia, A., Van de Put, M. L. & Vandenberghe, W. G. Dielectric properties of hexagonal boron nitride and transition metal dichalcogenides: from monolayer to bulk. *npj 2D Mater. Appl.* **2**, 6 (2018).
49. Baek, H. et al. Highly energy-tunable quantum light from moiré-trapped excitons. *Sci. Adv.* **6**, eaba8526 (2020).
50. Brotons-Gisbert, M. et al. Moiré-trapped interlayer trions in a charge-tunable $WSe_2/MoSe_2$ heterobilayer. *Phys. Rev. X* **11**, 031033 (2021).
51. Thompson, A. P. et al. LAMMPS—a flexible simulation tool for particle-based materials modeling at the atomic, meso, and continuum scales. *Comp. Phys. Comm.* **271**, 108171 (2022).
52. Soler, J. M. et al. The SIESTA method for ab initio order-*N* materials simulation. *J. Phys.: Condens. Matter* **14**, 2745 (2002).
53. Kohn, W. & Sham, L. J. Self-consistent equations including exchange and correlation effects. *Phys. Rev.* **140**, A1133–A1138 (1965).
54. Fernández-Seivane, L., Oliveira, M. A., Sanvito, S. & Ferrer, J. On-site approximation for spin-orbit coupling in linear combination of atomic orbitals density functional methods. *J. Phys.: Condens. Matter* **18**, 7999 (2006).
55. Troullier, N. & Martins, J. L. Efficient pseudopotentials for plane-wave calculations. *Phys. Rev. B* **43**, 1993–2006 (1991).
56. Papior, N., Lorente, N., Frederiksen, T., García, A. & Brandbyge, M. Improvements on non-equilibrium and transport Green function techniques: the next-generation TRANSIESTA. *Comput. Phys. Commun.* **212**, 8–24 (2017).

Acknowledgements

We thank J. Ruhman for insightful discussions. This work was supported by the EPSRC (grant nos. EP/P029892/1 and EP/L015110/1), and the ERC (grant no. 725920) (A.J.C., M.B.-G., H.B., T.V.I., A.B. and B.D.G). V.V. and J.L. acknowledge funding from the EPSRC (grant no. EP/S025324/1). This work used the ARCHER2 UK National Supercomputing Service via J.L.'s membership of the HEC Materials Chemistry Consortium of UK, which is funded by the EPSRC (EP/L000202). This project has received funding from the European Union's Horizon 2020 research and innovation programme under the Marie Skłodowska-Curie grant agreement no. 101067977. M.B.-G. is supported by a Royal Society University Research Fellowship. B.D.G. is supported by a Wolfson Merit Award from the Royal Society and a Chair in Emerging Technology from the Royal Academy of Engineering. K.W. and T.T. acknowledge support from JSPS KAKENHI (grant nos. 19H05790, 20H00354 and 21H05233).

Author contributions

A.J.C. performed the experimental measurements, except for the second-harmonic generation measurements which were performed by A.B. and T.V.I. A.J.C., M.B.-G. and B.D.G. analysed the data. H.B. fabricated the sample. V.V. and J.L. performed the theoretical calculations. T.T. and K.W. grew the hBN crystals. B.D.G. and J.L. conceived and supervised the project. A.J.C., V.V., M.B.-G, J.L. and B.D.G. wrote the paper with input from all authors.

Competing interests

The authors declare no competing interests.

Additional information

Extended data is available for this paper at https://doi.org/10.1038/s41567-024-02385-4.

Supplementary information The online version contains supplementary material available at https://doi.org/10.1038/s41567-024-02385-4.

Correspondence and requests for materials should be addressed to Brian D. Gerardot.

Peer review information *Nature Physics* thanks David Ruiz-Tijerina, and the other, anonymous, reviewer(s) for their contribution to the peer review of this work.

https://doi.org/10.1038/s41567-024-02385-4

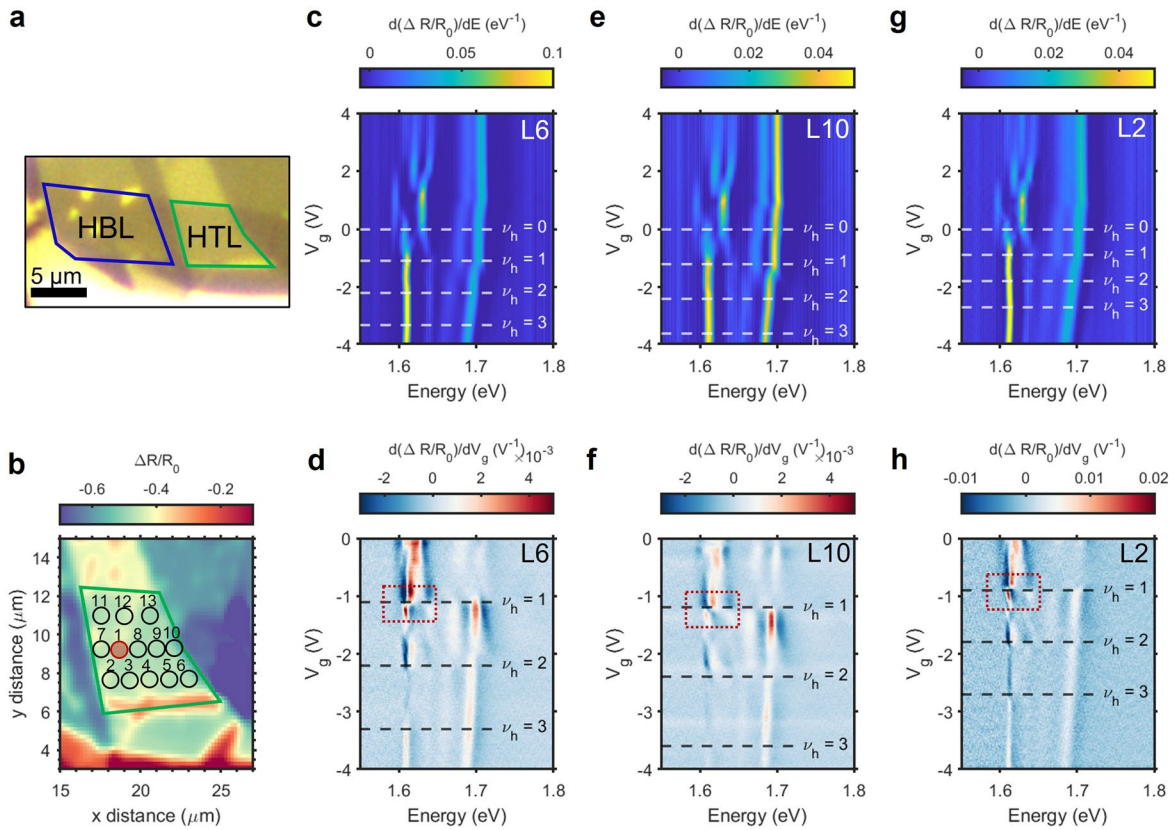

Extended Data Fig. 1 | Twist angle homogeneity in the heterotrilayer. **a** Optical micrograph of the stacked heterobilayer (HBL) and heterotrilayer (HTL) device regions before encapsulation in hBN. **b** Spatial map of the $\Delta R/R_0$ integrated in the spectral range 739 nm to 741 nm, with the HTL region outlined in green. The numbered spots indicate the measured locations. The red circle (L1) identifies the location measured in the main text. The lateral size of the spot indicates an estimate of the confocal collection spot size. **c** V_g dependence of $d(\Delta R/R_0)/dE$ in location 6 (L6) of the HTL. **d** ν_h dependence of the $d(\Delta R/R_0)/dV_g$ in L6. The dashed lines indicate integer fractional fillings of holes in each moiré unit cell. **e,f** As described for panels (c,d) for L10. **g,h** As described for panels (c,d) for L2. The dashed red boxes identify the highly reproducible signature that occurs for $\nu_h = 1$.

https://doi.org/10.1038/s41567-024-02385-4

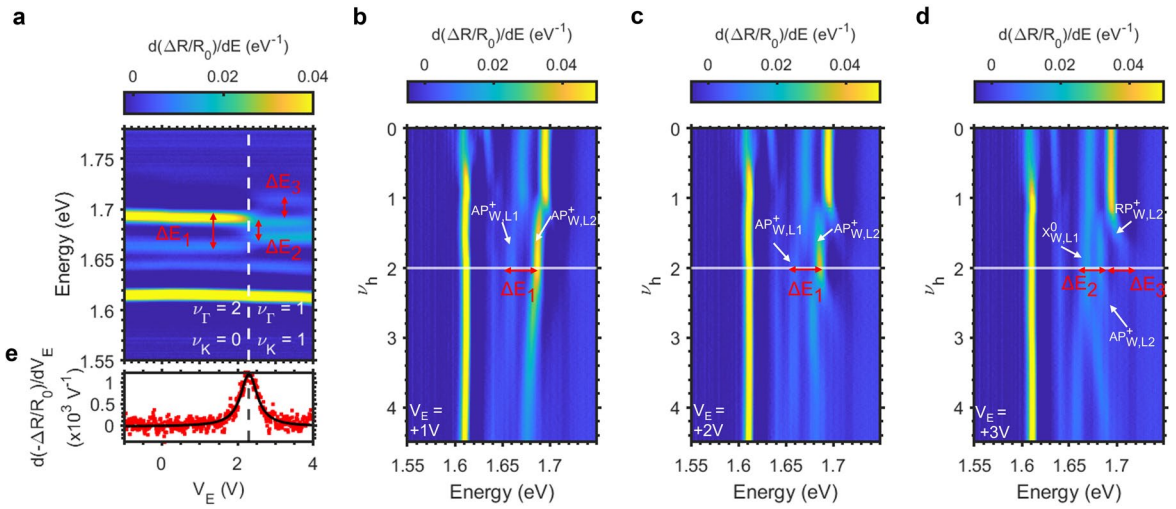

Extended Data Fig. 2 | Exciton-polaron behaviour under band realignment. a Density plot showing the V_E dependence of the $d(\Delta R/R_0)/dE$ when the hole filling is fixed at $\nu_h = 2$. The white dashed line indicates an abrupt change in the observed resonances. At $V_E = +2V$, ΔE_1 is estimated to be 25 meV, extracted from Lorentzian oscillator fits to the resonances. For $V_E = +3V$, ΔE_2 and ΔE_3 are found to be 21 meV and 15 meV respectively. **b-d** Density plots of the V_g dependence of $d(\Delta R/R_0)/dE$ when a constant V_E of + 1 V (b), + 2 V (c) and + 3 V (d) is applied. For $V_E = +1V$ and $V_E = +2V$, the energy splittings between $AP^+_{W,L1}$ and $AP^+_{W,L2}$ (ΔE_1) are found to be 23 meV and 24 meV respectively. This is in good agreement with the ΔE_1 estimated at $V_E = +2$ V in panel (a). As previously shown in the main text, the direct momentum electron-hole pairs at ± K are dressed by holes resident in the Γ derived moiré valence band, forming a correlated state ($\nu_\Gamma = 2$, $\nu_K = 0$). For $V_E = +3V$ and $\nu_h = 2$, the energy splitting between $X^0_{W,L1}$ and $AP^+_{W,L2}$ (ΔE_2) is measured to be 15 meV, while the splitting between $AP^+_{W,L2}$ and $RP^+_{W,L2}$ (ΔE_3) is measured to be 24 meV. These are close to the values extracted for ΔE_2 and ΔE_3 in panel a, and hence allow us to identify the three resonances for $V_E > +2.3$V as $X^0_{W,L1}$, $AP^+_{W,L2}$ and $RP^+_{W,L2}$ in order of increasing energy. As previously shown by the polarisation resolved measurements under an applied magnetic field (Fig. 3a,b in the main text) for $V_E = +3V$, $AP^+_{W,L2}$ is formed by an exciton dressed by holes in the moiré band deriving from ± K point in L2. We therefore determine that at $V_E = +2.3V$ in panel a the holes in the Γ_B orbital are suddenly transferred to the L2 K orbital, forming a correlated state with $\nu_\Gamma = 1$ and $\nu_K = 1$. **e** To characterise the abruptness of the hole transfer, we fit the full width half maximum of the $d(\Delta R/R_0)/dV_E$ at 1.68 eV. The solid black line represents a Lorentzian fit to the data, from which a full width half maximum of 0.53 V is extracted, centred around $V_E = 2.30$ V.

https://doi.org/10.1038/s41567-024-02385-4

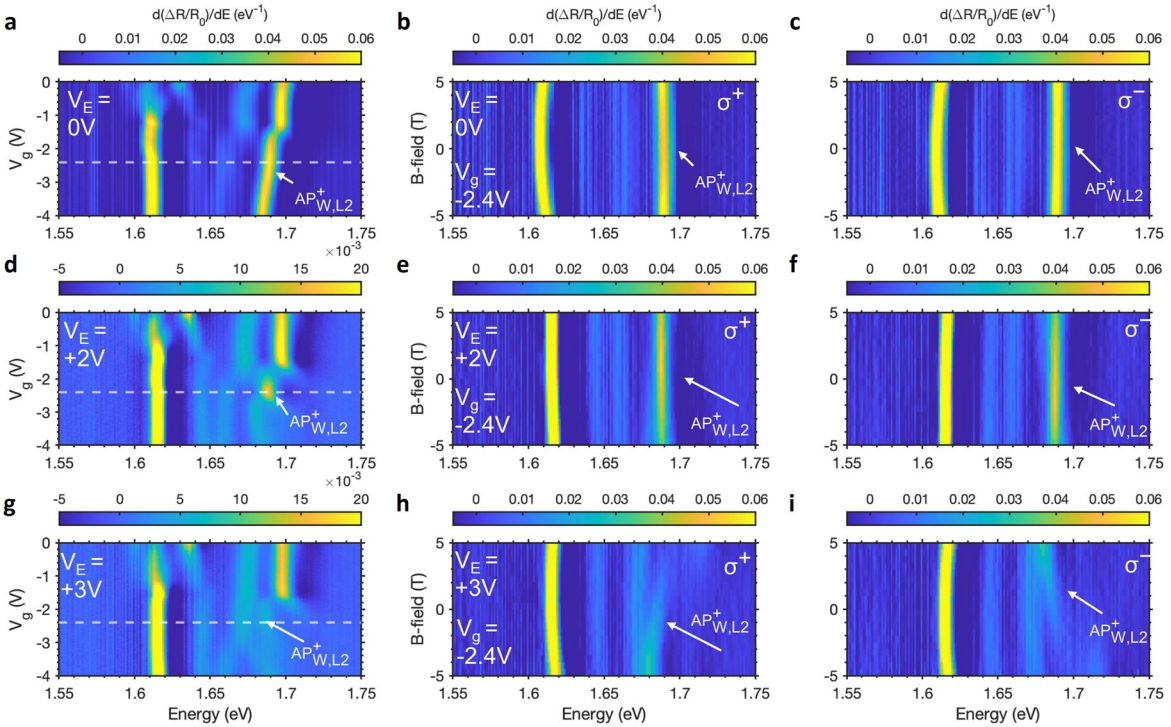

Extended Data Fig. 3 | Enhancement of magnetic interactions for K orbital holes. a, V_g dependence of d($\Delta R/R_0$)/dE at V_E = 0V. The white arrow indicates the L2 WSe_2 attractive polaron resonance. **b,c** σ^+ (b) and σ^- resolved B-field sweep of d($\Delta R/R_0$)/dE at V_E = 0 V and V_g = − 2.4 V as indicated by the white dashed line in panel (a). **d-f**, As described for panels (a-c) for V_E = +2 V. **g-i** As described for panels (a-c) for V_E = +3 V. For V_g = − 2.4 V for both V_E = + 0 V and V_E = +2 V (ν_Γ ~ 2, ν_K = 0) the attractive polaron formed from the exciton in the upper WSe_2 layer (L2) $AP^+_{W,L2}$ exhibits a very small shift in energy with magnetic field. In contrast, for V_E +3 V, and V_g = − 2.4 V (ν_Γ ~ 1, ν_K ~ 1) $AP^+_{W,L2}$ exhibits both a huge positive g-factor and a large degree of spin polarisation, consistent with carriers loaded at the ± K points.

https://doi.org/10.1038/s41567-024-02385-4

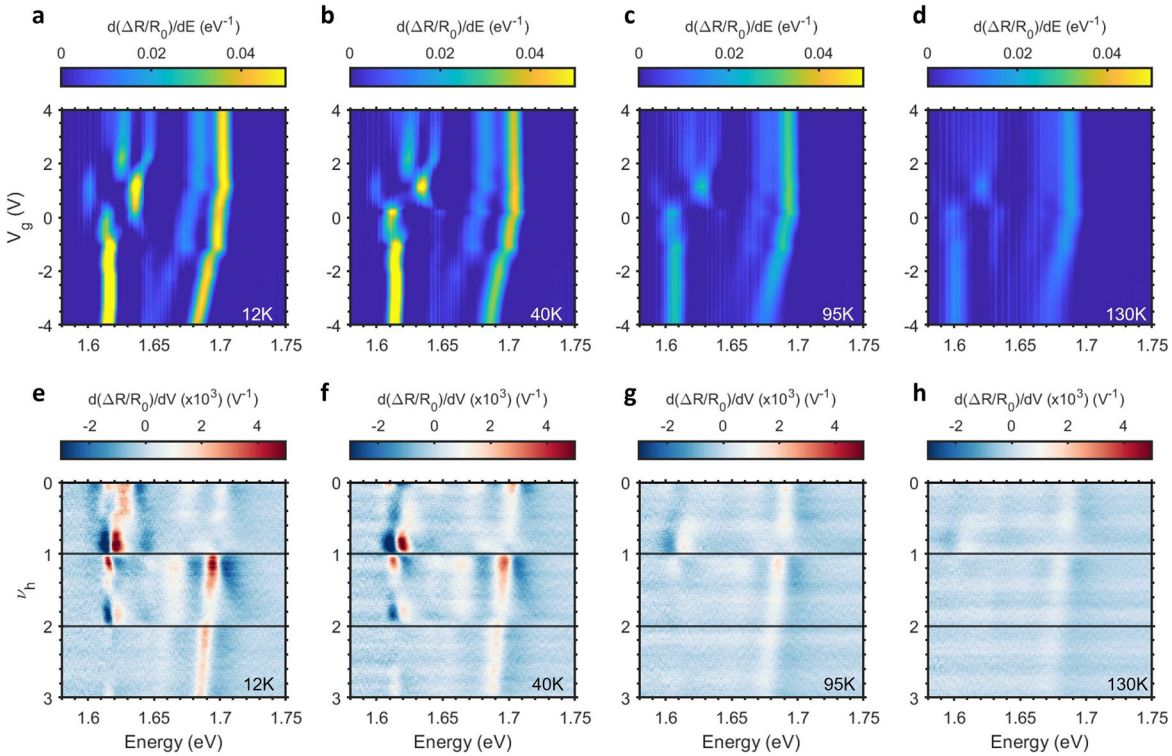

Extended Data Fig. 4 | Temperature dependence of the strongly correlated electronic states in the heterotrilayer. a, V_g dependence of $d(\Delta R/R_0)/dE$ at a sample temperature of 12 K, **b** 40 K, **c** 95 K and **d** 130 K. **e** ν_h dependence of $d(\Delta R/R_0)/dV_g$ at 12 K, **f** 40 K, **g** 95 K and **h** 130 K. The abrupt changes in the $d(\Delta R/R_0)/dV_g$ signal that indicate the formation of correlated hole states disappear as the temperature is increased.

https://doi.org/10.1038/s41567-024-02385-4

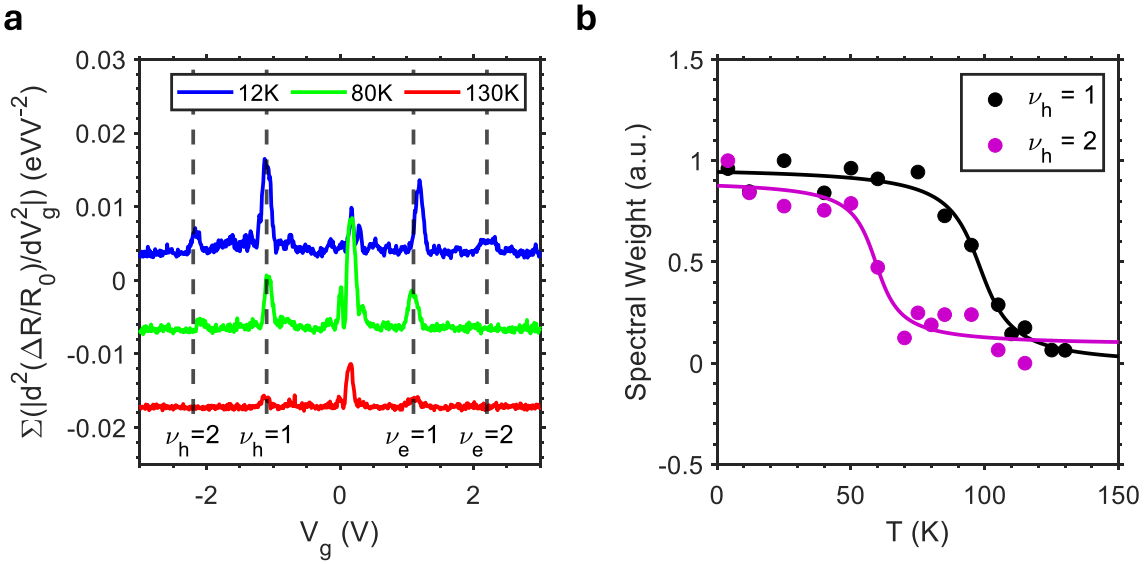

Extended Data Fig. 5 | Analysis of the temperature dependence of strongly correlated electronic states in the heterotrilayer. a, Second derivative of $\Delta R/R_0$ with respect to V_g integrated in the spectral range 1.59 to 1.76 eV for different temperatures. We observe peaks in $\Sigma|\,d^2(\Delta R/R_0)/\,d^2V_g|$ at $\nu_{e,h} = \pm 1, \pm 2$. We fit the peaks at $\nu_h = 1, 2$ using a Gaussian and integrate the peak area to provide an estimate of the strength of the correlated states at $\nu_h = 1, 2$. **b**, Evolution with temperature of the normalised integrated area of the peaks at $\nu_h = 1, 2$ in $\Sigma\,(|\,d^2(\Delta R/R_0)/dV_g^2|$ (indicated by the vertical dashed lines). By fitting an arctan function to the temperature dependence of the normalised spectral weight, we estimate the temperature T_C at which the strongly correlated states disappear. We find T_C ~ 98 K for $\nu_h = 1$ and T_C ~ 59 K for $\nu_h = 2$. The T_C for $\nu_h = 1$ corresponds to a charge gap of 8.4 meV.

https://doi.org/10.1038/s41567-024-02385-4

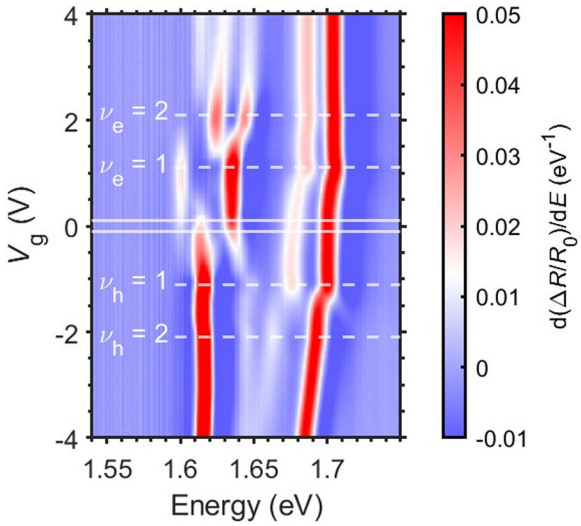

Extended Data Fig. 6 | Charge neutrality region in the heterotrilayer. V_g dependence of the $d(\Delta R/R_0)/dE$ signal in the heterotrilayer. The solid white lines indicate the charge neutrality region, while the dashed lines indicate where correlated states are formed at integer fillings of the moiré superlattice. The labelling of the charge neutrality region is omitted in the main manuscript to avoid over-crowding the figure.

https://doi.org/10.1038/s41567-024-02385-4

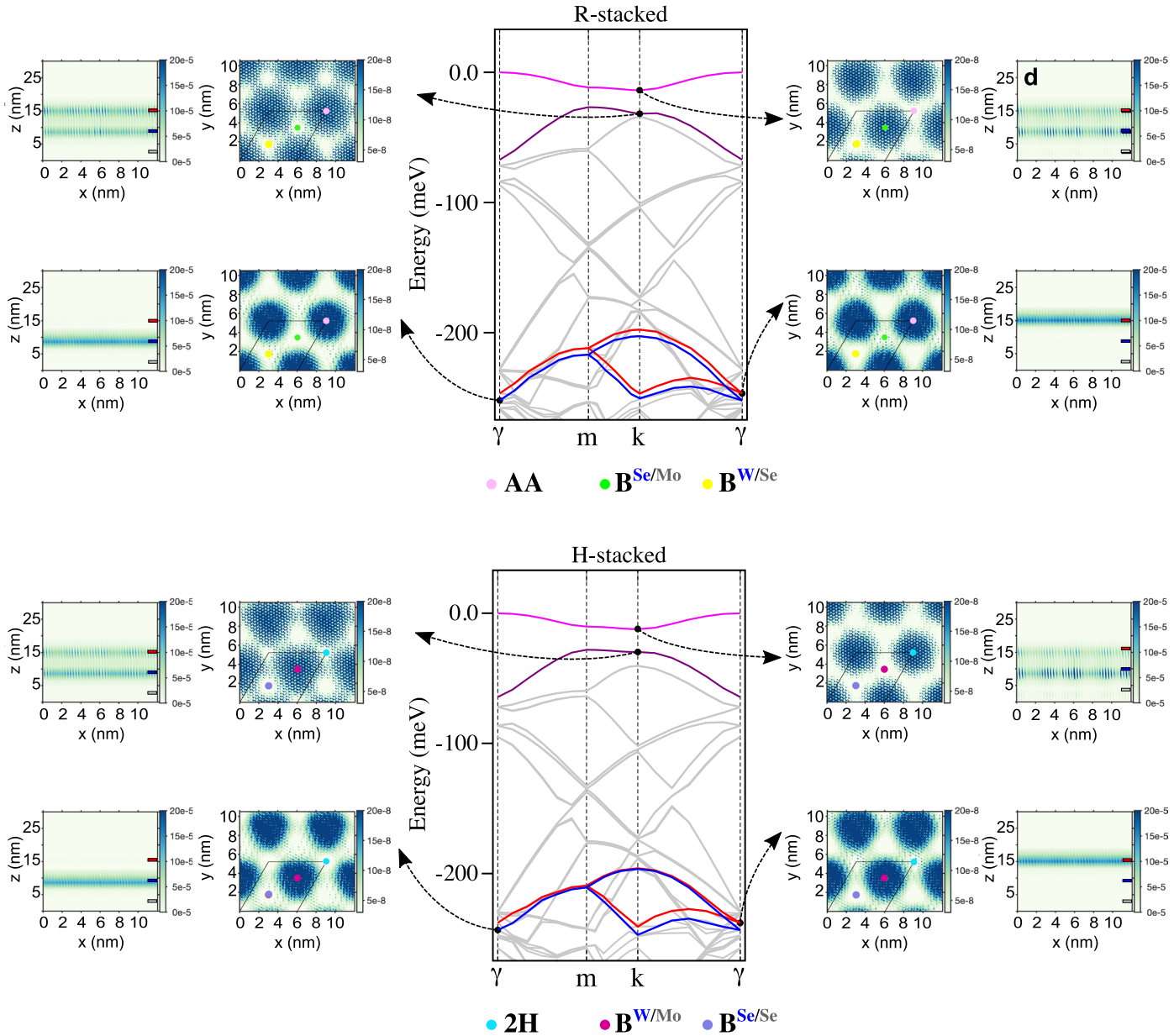

Extended Data Fig. 7 | DFT calculations for R- versus H-stacking. Top valence bands and wavefunction densities at high-symmetry points for two different stackings of a 2H-WSe_2 bilayer on a twisted $MoSe_2$ layer. Top two valence bands derive from Γ valley of WSe_2 and are labeled as Γ_A (top, light purple) and Γ_B (bottom, dark purple). Bands deriving from ± K valley of WSe_2 are also highlighted in red and blue, respectively. See the main manuscript for more details. Top panel: R-stacked ($\theta = 3.1^{\circ}$). Wavefunction densities of Γ_A and Γ_B bands at the k valley of the moiré BZ and of $K(L_1)$ and $K(L_2)$ at the γ valley of the moiré BZ. Bottom panel: same as top valley but for H-stacked ($\theta = 56.9^{\circ}$). For twisted homobilayers (for example WSe_2) R-stacking is necessary to obtain ground state Γ-derived moiré bands with a honeycomb lattice[20,27]. However, in the case of the monolayer $MoSe_2$ / 2-H natural WSe_2 bilayer (HTL) device, we find that DFT calculations cannot distinguish between R- and H-stacked HTLs in terms of band structure and localization of wavefunctions. As shown in the figure we find that the two different configurations result in very similar electronic band structures at the top of the valence manifold. Moreover, even though R-stacked and H-stacked HTLs exhibit different stacking types, the relative localization of states from Γ_A, Γ_B and K(L2) is the same for both HTLs: in particular, states from Γ_B and K(L2) are localized in the same regions resulting in the same predictions for optical properties of both HTLs.

https://doi.org/10.1038/s41567-024-02385-4

Extended Data Table 1 | Summary of the twist angle homogeneity in the heterotrilayer region

Sample Location	ΔV_g ($\nu_h = 1$)	Twist angle (°)
1	1	2.7
2	0.9	2.6
3	1.15	2.9
4	1.15	2.9
5	0.9	2.6
6	1.1	2.8
7	1.1	2.8
8	1.1	2.8
9	1.15	2.9
10	1.2	2.9
11	1.15	2.9
12	1.1	2.8
13	1.1	2.8

For each spatial location shown in Extended Data Figure 1, we identify the gate voltage offset from charge neutrality, ΔV_g, required to fill the moiré superlattice with one hole per site (ν_h=1) and extract a local twist angle from this value using the parallel plate capacitor model. We measure an average twist angle of 2.8° with a total variation of 0.4° across the full HTL region.

https://doi.org/10.1038/s41567-024-02385-4

Extended Data Table 2 | Summary of the magnetic interactions for Γ- versus K orbital holes

V_E (V)	V_g (V)	ν_h	Orbital of holes at E_F	g-factor $AP^{+}_{W,L2}$
0	-2.4	2.3	Γ	-3.4 ± 0.1
0	-3.5	3.4	Γ	-1.1 ±0.1
+2	-2.4	2.1	Γ	3.5±0.3
+2	-3.5	3.2	K	62 ± 3
+3	-1.9	1.5	K	29 ± 1
+3	-2.4	2	K	49 ± 2
+3	-3.5	3.2	K	63 ± 1

Measured g-factors of the WSe_2 hole dressed attractive polaron $AP^{+}_{W,L2}$ for different values of V_E and V_g for which the holes at the Fermi level (E_F) occupy either a Γ or K orbital. The g-factor is enhanced when the holes occupy a K orbital.